A Journal of the Gesellschaft Deutscher Chemiker

Angewandte International Edition GDCh Chemie

www.angewandte.org

Accepted Article

Title: A Triatomic Cobalt Catalyst for Oxygen Electrocatalysis

Authors: Tianmi Tang, Xiaoqin Xu, Xue Bai, Changmin Hou, Zhenlu Wang, Tao Gan, and Jingqi Guan

To be cited as: *Angew. Chem. Int. Ed.* **2025**, e202503019

Link to VoR: https://doi.org/10.1002/anie.202503019

WILEY VCH

RESEARCH ARTICLE

WILEY VCH

A Triatomic Cobalt Catalyst for Oxygen Electrocatalysis

Tianmi Tang[a], Xiaoqin Xu[a], Xue Bai[a], Changmin Hou[b], Tao Gan[c], Zhenlu Wang[a], and Jingqi Guan*[a]

[a] T. Tang, X. Xu, X. Bai, Z. Wang, J. Guan*
Institute of Physical Chemistry
College of Chemistry, Jilin University
2519 Jiefang Road, Changchun 130021, P. R. China
E-mail: guanjq@jlu.edu.cn

[b] H. Hou
State Key Laboratory of Inorganic Synthesis and Preparative Chemistry
College of Chemistry, Jilin University
Changchun 130021, P. R. China

[c] T. Gan
Shanghai Synchrotron Radiation Facility
Shanghai Advanced Research Institute, Chinese Academy of Sciences
Shanghai, China

Supporting information for this article is given via a link at the end of the document.

Abstract: The advancement of rechargeable zinc-air batteries significantly depends on bifunctional oxygen electrocatalysts to provide outstanding oxygen reduction/evolution reaction (ORR/OER) performance. However, it is still challenging to design electrocatalysts with excellent bifunctional activity and stability. Here, we adopt an ultrafast printing method to efficiently embed a tri-atom cobalt complex precursor onto graphene nanosheets to obtain a triatomic catalyst (Co_3-NG), exhibiting a durable and excellent bifunctional catalyst in the electrocatalytic ORR ($E_{half\text{-}wave}$ = 0.903 V) and OER ($E_{j=10}$ = 1.596 V). The Co_3-NG-assembled zinc-air battery can output a maximum power density of 189.0 mW cm^{-2} at 330 mA cm^{-2} and can be charged and discharged over 3,000 cycles significantly outperforming the Pt/C+RuO_2 benchmark (146.5 mW cm^{-2}, 360 cycles) under testing conditions of 25 °C. *In situ* XAS analysis and theoretical calculations unclose that Co_3ON_6 is the catalytic site for bifunctional ORR/OER electrocatalysis. The constructed triangular pyramidal active sites effectively regulate the *d*-band center and electronic configuration, and promote the adsorption/desorption of oxygen intermediates. This work uncovers that the geometry and electronic structure of triatomic active center play a key role in improving bifunctional ORR/OER performance for electrochemical energy applications.

Introduction

Rechargeable zinc-air batteries (ZABs) show a large theoretical energy density (1086 Wh kg^{-1}), cost effectiveness, environmental benignity and high safety, making them potential candidates for next-generation energy storage and conversion facility.[1] The ORR in the discharge process and OER in the charging process of ZABs are mutually reversible, showing slow kinetic and high energy barrier, thus impeding the energy efficiency.[2] Currently, commercial ORR and OER catalysts are mainly Pt-, Ir- or Ru-based precious metal catalysts, but their single function, poor stability and high cost limit the large-scale application.[3] Therefore, researchers have begun to work on the development of inexpensive and efficient bifunctional catalysts.

In recent years, single-atom catalysts (SACs), characterized by their 100% atom utilization and uniform active-site configuration, spark profound interest as viable Pt/C alternatives.[4] By manipulating the coordination environments surrounding active single atoms, the energy barriers for proton-electron transfer processes can be selectively altered, providing an optimal setting for investigating the relationship between the structure and ORR/OER activity.[5] Nonetheless, in the case of multi-electron transfer reactions, the isolated nature of single sites within SACs poses challenges in overcoming the linear scaling relationship between their adsorption strength and various intermediates, such as multiple oxygen-containing species (*OOH, *O, and *OH) with differing binding preferences.[6] Diatomic catalysts (DACs) as the extension of SACs can break the linear relationship. The adjacent two metal centers not only optimize the electron configuration of the active site through short-range electron interactions, but also provide a new location for the reaction intermediates.[7] Previous studies have shown that in single-atom configurations, the O_2 adsorption mode is end-on configuration and the binding pathway is more likely to occur, while in diatomic configurations, the O_2 adsorption mode is preferentially bridge-cis-configuration and the dissociation pathway is more likely to occur.[8] Compared with the association pathway, the dissociation pathway can directly split the O–O bond to achieve rapid four-electron transfer in one step, and effectively improve the oxygen conversion efficiency and ORR kinetics.[9] For instance, Fe-Co dual-atom sites incorporated within N-enriched graphene presented higher ORR activity and stability involving the division barrier of O_2 and OOH into O and OH as low as 0.25 and 0.02 eV, respectively, significantly lower than those observed on individual Fe or Co sites.[10]

Although DACs have achieved significant progress, offering two adjacent metal atoms and greater degrees of freedom than SACs, the geometric and electronic properties of the diatomic configuration can not fully optimize the adsorption energies for

all intermediates. Furthermore, uncovering the configuration-activity relationships, elucidating the synergistic enhancement mechanisms of heteroatomic sites, and understanding their inherent bifunctional properties remain significant challenges.[11] It has been reported that triatomic catalysts (TACs),[12] in which tri-atom active sites are not the simple sum of single atom sites and diatomic sites, have different catalytic properties, and there may be synergistic effects to break through the theoretical limits of SACs and DACs owing to the more freedom for adsorbed species.[13] Through extensive ab initio calculations focusing on trimers of 3d, 4d, and 5d transition metals, Zhou et al. illuminated that these spatially constrained triatomic metal clusters possess the ability to simultaneously bind multiple CO_2 molecules and offer distinctive reaction pathways that spatially and electronically facilitate C–C coupling.[14] Based on theoretical calculations, Shui et al. demonstrated higher activity of precious TACs than SACs.[15] The electron structure showed that the O-2p and Pt-3d orbitals have strong hybrid strength in the system of OH adsorption on Pt_3-NG, which is conducive to the electrocatalytic reaction. In addition, Wu et al. constructed a trinuclear active structure (Co_2MnN_8) that can spontaneously combine with OH to form Co_2MnN_8-2OH, which generates a half-filled d_{z^2} orbital that easily penetrates the antibonding π orbital of oxygen, thus promoting the adsorption or desorption of oxygen-containing intermediates in the ORR.[16] Hence, it is an effective way to design bifunctional OER/ORR catalysts based on the structure of TACs.

Among the transition metals studied, Fe or Co embedded onto N-doped carbon substrates to form the M-N-C materials are recognized to be the most promising oxygen electrode catalysts.[17] However, the deleterious Fenton reactions (Fe^{2+} + H_2O_2) of Fe-N-C materials limit their practical applications.[18] Therefore, improving the ORR activity of Co-N-C has become an important goal in the development of ORR electrocatalysts. Studies have shown that Co–N_x sites can significantly affect ORR/OER activity, and the catalytic performance can be improved by adjusting the coordination environment of cobalt active centers.[19] However, the construction of triatomic active sites through directional controlled synthesis still face a huge challenge, and the key problem is to inhibit the aggregation of atoms caused by high surface energy. Although some literatures have reported the synthesis of DACs by encapsulation-pyrolysis method, using porous materials to encapsulate macrocyclic complexes, and then retaining the main carrier of molecular framework through pyrolysis to obtain the target catalysts,[20] the method of accurately and controllably synthesizing TACs still needs to be explored, since during the encapsulation process, the target metal ions would be exchanged with the ions for the synthesis of porous materials in the solution and the triatomic structure might be destroyed.

For more controlled synthesis of TACs, we developed an ultrafast printing method that can effectively inhibit atom migration and accurately synthesize the target triatomic active sites. In this method, the pre-synthesized triatomic cobalt complex precursor was adsorbed onto the support by electrostatic action, and nitrogen-doped triatomic cobalt catalyst (Co_3-NG) is then obtained by ultrafast Joule heat pyrolysis. The Co_3-NG catalyst demonstrates fantastic ORR and OER performance with ORR half-wave potential ($E_{1/2}$) of 0.903 V and OER overpotential (η_{10}) of 366 mV. The assembled Co_3-NG-based zinc-air battery can be continuously charged and discharged for over 3,000 cycles. *In situ* X-ray absorption spectroscopy (XAS) and theoretical simulation findings show that the construction of Co_3ON_6 active site with triangular pyramidal configuration effectively regulates the adsorption mode and d-band center of reaction intermediates, which makes the catalyst have good ORR/OER bifunctional activity.

Results and Discussion

Synthesis and characterization

Figure 1a displays the ultrafast printing method for the synthesis of the triatomic cobalt catalyst onto N-doped graphene (Co_3-NG). The term "ultrafast printing" describes the rapid anchoring of the Co_3 clusters onto the graphene substrate. First, a cobalt cluster complex (Co_3L) was synthesized by a recrystallization method.[21] The trimer cobalt atoms are all coordinated to a pyridine ligand, and three adjacent Co atoms are bridged with oxygen to give a highly central coordination structure (Figure S1). The detailed crystal structure was illustrated by Fourier transform infrared (FTIR) spectroscopy examination (Figure S2), indicating the successful synthesis.[22] The synthesized Co_3L was electrostatically absorbed on graphene oxide (GO), and the suspension liquid was freeze-dried to produce the precursor of Co_3L-GO. To control the rate of atomic migration, the Co_3L-GO was fleetly annealed within two seconds in NH_3 atmosphere and then cooled down in liquid nitrogen. For comparison, diatomic cobalt-doped graphene (Co_2-NG) and single-atom Co-doped graphene (Co_1-NG) were synthesized using similar methods as depicted in the supporting information, and the structures of Co_2L, Co_2-NG and Co_1-NG are shown in Figure S3. Transmission electron microscopy (TEM) images reveal that Co_3-NG exhibits a morphology of 2D ultrathin nanosheets and no visible nanoparticles (Figure 1b, c). The energy dispersive spectrometer (EDS) mappings of Co_3-NG clearly demonstrate that the Co, N, O, and C elements are uniformly over the whole NG (Figure 1d, e). Furthermore, the atomic configuration of Co within the Co_3-NG catalyst is verified by aberration-corrected high-angle annular dark-field scanning transmission electron microscopy (AC-HAADF-STEM) images (Figure 1f, g and Figure S4), and the existence of bright spots indicates that the Co atoms are successfully anchored and evenly dispersed on the graphene substrate. In particular, triangular triatomic configuration can be seen, enlightening the speculation of trimeric sites. When analyzing the local environment, it is observed that the adjacent Co atoms form a triangular structure, and their direct distances are 2.6 Å, 2.7 Å, and 3.8 Å, respectively (Figure 1h, i). Besides, the intensity distributions of line profile show that the spacing between adjacent Co atoms are mainly ~2.6 Å and 3.8 Å (Figure 1j), demonstrating the successful construction of the triatomic cobalt structure.

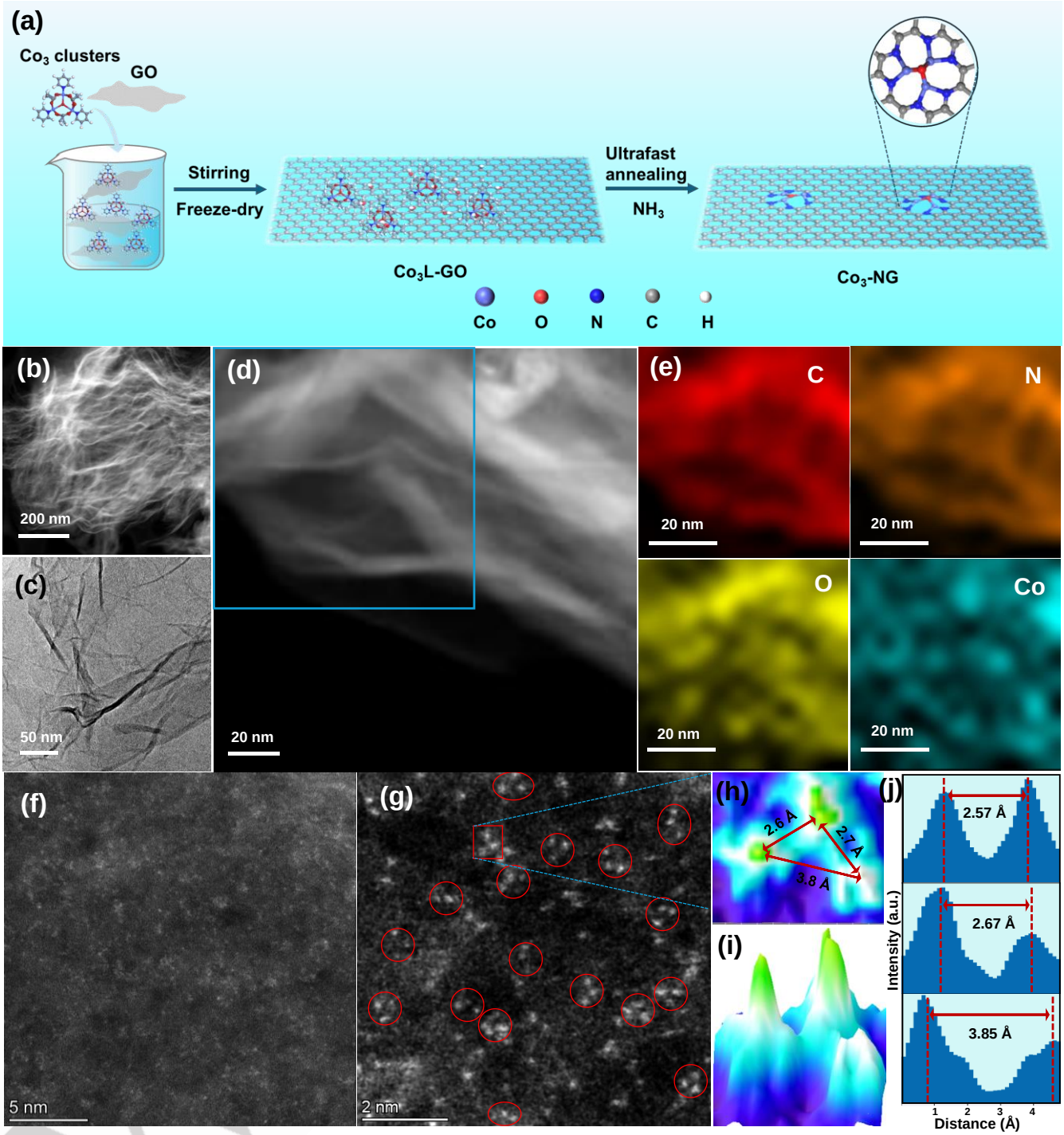

Figure 1. (a) Synthesis diagram of Co_3-NG. (b, c) HRTEM images. (d) HRTEM and (e) the corresponding EDS mapping. (f, g) Aberration-corrected HAADF-STEM images. (h-j) Interatomic distance assessment.

The crystal structures of Co_3-NG, Co_2-NG and Co_1-NG were analyzed by X-ray diffraction (XRD), showing two obvious peaks positioned approximately at 26.4° and 43.4°, which belong to the graphene matrix (Figure S5). There are no detectable Co particle signals, meaning that the Co species are highly dispersed in the three catalysts.[23] The graphitic degrees of the catalysts were acquired through Raman spectroscopy, as depicted in Figure S6. Two distinct broad peaks situated roughly at 1345 and 1590 cm^{-1} correspond to the D band and G band, respectively.[24] The intensity ratio of the D band to the G band (I_D/I_G) for NG is 1.08, which is higher than that of Co_3-NG (0.98), Co_2-NG (1.01) and Co_1-NG (1.06), implying that the doping of Co can improve the graphitization degree of carbon substrate and reduce defects. The degree of graphitization of carbon substrate reflects the electron transfer ability, and the electron transfer in the Co_3-NG is better than NG, Co_1-NG and Co_2-NG.[25] X-ray photoelectron spectroscopy (XPS) was employed to investigate the constituent elements and the oxidation state of Co in the catalysts. The XPS survey spectra of Co-NG, Co_2-NG and Co_3-NG reveal the presence of C, N, O and Co, as shown in

Figure S7. The Co 2p spectra of Co_1-NG, Co_2-NG and Co_3-NG demonstrate peaks at 780.8, 781.4 and 781.6 eV, respectively, indicating that they have a valence state close to +2 (Figure 2a).[26] Further comparison of Co $2p_{3/2}$ among the three catalysts shows that Co_3-NG exhibits higher binding energy, indicating that the electron density of Co atoms can be modulated by the coordination environment.[27] The high-resolution N 1s spectra of Co_1-NG, Co_2-NG and Co_3-NG were deconvolved into five characteristic peaks, which are assigned to pyridinic–N, Co–N, pyrrolic–N, graphitic–N and oxidized–N, positioned at 398.6 eV, 399.3 eV, 400.1 eV, 401.2 eV, and 404.0 eV, respectively (Figure 2b), indicating the presence of Co–N in all three samples.[28] Co-N_x sites are known to enhance both ORR and OER activities. Pyridine–N within the active site contributes to ORR activity, while graphitic–N improves electron transfer efficiency, thereby accelerating the overall catalytic performance.[29]

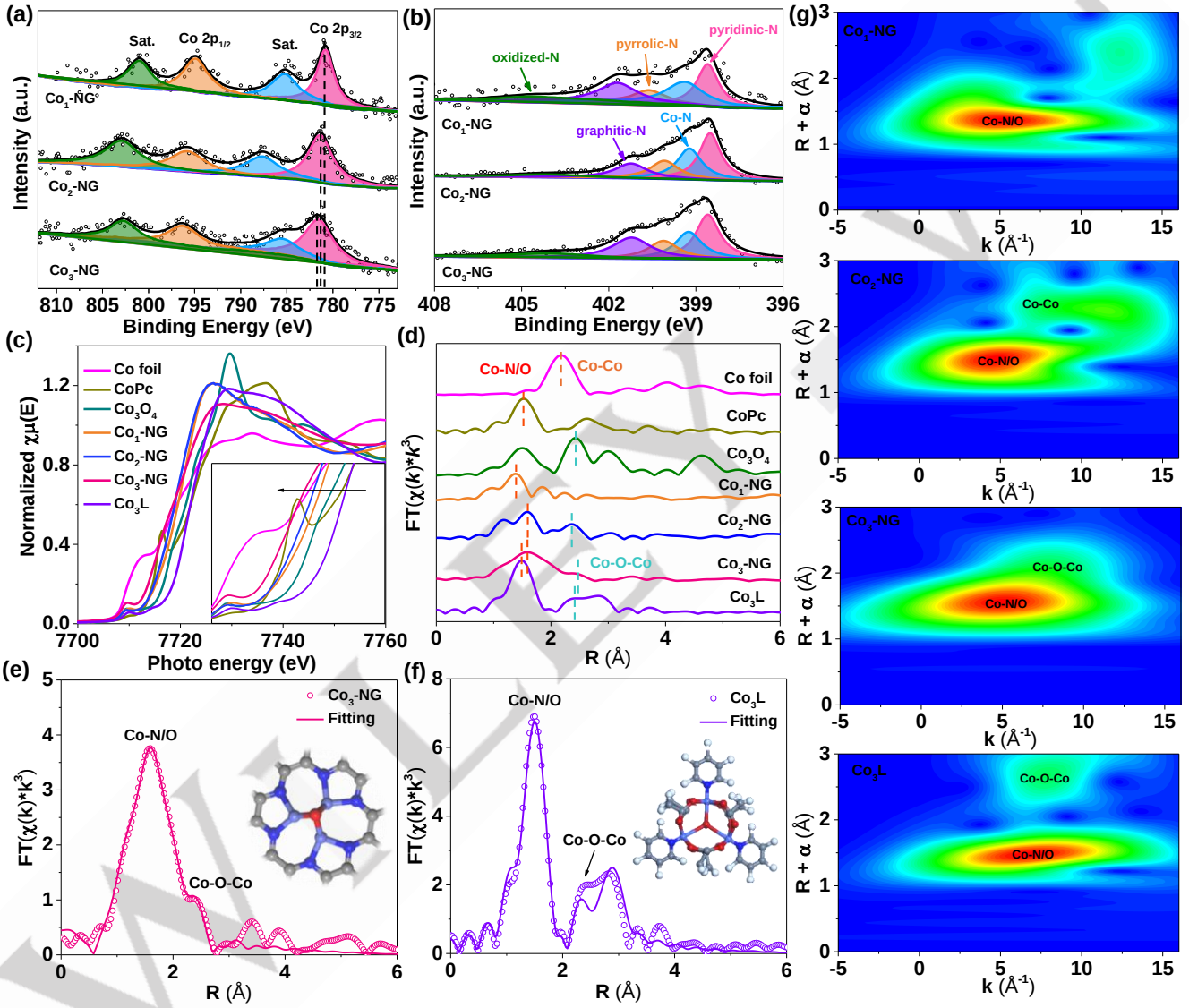

Figure 2. (a) Co 3d and (b) N 1s XPS spectra of Co_1-NG, Co_2-NG and Co_3-NG. (c) Co k-edge XANES spectra of Co foil, CoPc, Co_3O_4, Co_1-NG, Co_2-NG, Co_3-NG and Co_3-L samples. (d) FT-EXAFS spectra. (e, f) FT-EXAFS of the R-space fitting curve for Co_3-NG and Co_3-L (Inset: model of Co_3-NG and Co_3-L). (g) WT-EXAFS plots.

The oxidation state and coordination structures were further surveyed by XAS.[30] As shown in Co K-edge X-ray absorption near-edge structure (XANES) spectra (Figure 2c), the absorption edge for Co_1-NG, Co_2-NG, and Co_3-NG is very close to that of cobalt phthalocyanine (CoPc), suggesting that the oxidation state of cobalt in these samples is approximately +2. Moreover, the absorption edge of Co_3-NG is more negative than Co_1-NG and Co_2-NG, meaning that the oxidation state of Co in Co_3-NG is slightly lower in agreement with the aforementioned XPS results. In contrast, Co_3L exhibits an absorption edge higher than that of Co_3O_4, implying that the oxidation state of cobalt in Co_3L is higher than +2.7.[31] The The Fourier transform extended X-ray absorption fine structure (FT-EXAFS) reveals significant differences in the local coordination environment of Co across

the various catalysts, as shown in Figure 2d. The FT-EXAFS curves of the Co_1-NG, Co_2-NG, Co_3-NG and Co_3L catalysts exhibit a prominent peak at ~1.5 Å, corresponding to the Co-N/O coordination.[32] The peaks at ~2.4 Å in the FT-EXAFS spectra of Co_3-NG and Co_3L align closely with the Co–O–Co scattering path observed in Co_3O_4 reference, while differing from the Co–Co scattering path in Co foil.[33] The corresponding FT-EXAFS fitting curves and parameters (Figure 2e, Figure S8e and Table S1) reveal that the spectrum of Co_3-NG is well fitted with backscattering paths of Co–N and Co–O. Specifically, the coordination numbers for Co–N and Co–O are ~2.2 and ~0.9, respectively, and the corresponding bond length is ~1.81 Å and ~1.91 Å.[34] Furthermore, the bond length of Co–Co in the Co–O–Co path is ~2.56 Å, and the coordination number is ~1.1.[28] This result is consistent with the results obtained for the Co_3L (Figure 2f, Figure S8f and Table S1). The fitting results of Co_1-NG and Co_2-NG are shown in Figure S8a-d and Table S1, and the local coordination environment corresponds to Co_2N_6 and Co-N_4, respectively. The wavelet transform (WT) EXAFS analysis is utilized to effectively discriminate and identify the backscattering atoms within the local atomic structure. The WT plots for Co_3-NG and the reference samples are shown in Figure 2g and Figure S9. The maximum intensity of Co_3-NG is ~5.0 A^{-1}, which aligns with the Co–N/O coordination, while another maximum intensity, occurring at ~8.5 A^{-1}, matching with Co–O–Co scattering.[19c] Based on the fitting results, the coordinated environment of the triatomic cobalt in Co_3-NG can be reasonably assigned as Co_3ON_6 as illustrated in the inset of Figure 2e. The successful construction of Co_3ON_6 is attributed to Co_3-L acting as a precursor, providing Co metal sites initially coordinated with O and N atoms. Additionally, ammonia, as a nitrogen source, supplies active nitrogen species through high-temperature decomposition, which further react with Co metal centers to form Co-N bonds.[35]

Oxygen electrocatalysis performance

Cyclic voltammetry (CV) and linear sweep voltammetry (LSV) were applied to ascertain the catalytic ORR performance of the catalysts in 0.1 M KOH solution saturated with O_2. CV curves of Co_3-NG, Co_2-NG and Co_1-NG exhibit a pronounced reduction peak at 0.7 ~ 1.0 V vs. RHE, suggesting that all the samples possess ORR electrocatalytic performance (Figure S10).[36] Moreover, the Co_3-NG exhibits more positive reduction peak than Co_2-NG and Co_1-NG, illustrating higher ORR activity of the former. LSV curves illustrate that the Co_3-NG exhibits favorable onset and half-wave potentials (E_{onset} = 1.012 V and $E_{1/2}$ = 0.903 V), which are significantly superior to those of Co_2-NG (0.974 and 0.855 V), Co_1-NG (0.889 and 0.834 V), NG (0.873 and 0.663 V) and Pt/C (0.952 and 0.839 V) (Figure 3a).The diffusion limited current density (J_{lim}) of Co_3-NG at 0.5 V is −5.59 mA cm^{-2}, surpassing that of Pt/C (−4.66 mA cm^{-2}), Co_2-NG (−4.52 mA cm^{-2}), Co_1-NG (−3.62 mA cm^{-2}) and NG(−2.85 mA cm^{-2}), demonstrating its exceptional mass transport properties and intrinsic catalytic activity.[37] Moreover, the mass activity of Co_3-NG is significantly higher than that of the reference samples, further demonstrating its superior intrinsic catalytic activity (Figure S11).[38] The Tafel slope of Co_3-NG is 67 mV dec^{-1}, which compares favorably to those of Co_2-NG (84 mV dec^{-1}), Co_1-NG (80 mV dec^{-1}), NG (125 mV dec^{-1}) and Pt/C (90 mV dec^{-1}), implying that Co_3-NG has more beneficial ORR catalytic kinetics (Figure 3b).[39] In addition, the effect of cobalt content (Figure S12) and annealing temperature (Figure S13) on the ORR activity was studied. The catalytic activity is best when the cobalt doping amount was 1.0 *wt.*% and the annealing temperature is 1500 ℃. The results demonstrate that the catalyst achieves an optimal balance between the number of active sites and the dispersion of Co atoms, maximizing the formation of Co_3 active sites and ensuring proper graphitization of the carbon framework on this condition. This leads to an increased number of active sites and enhanced electron transfer capability, resulting in exceptional ORR performance.[40] The ORR performance of the synthesized Co_3-NG exhibits superiority compared to the majority of recently reported Co-based atomic catalysts (Table S3).The Koutecky-Levich (K-L) equation was used to evaluate approximate the electron transfer number (n) in the ORR.[41] The LSV curves were collected in the range of 400 to 2500 rpm min^{-1}, wherein the limit current density of Co_3-NG exhibits a gradual increase with increasing rotational speed (Figure 3c). The K-L diagram of Co_3-NG at 0.3 ~ 0.7 V determines that the average n is approximately 3.91, signifying that the ORR is predominantly a $4e^-$ pathway. Figure 3d illustrates the H_2O_2 yield and n of Co_3-NG and Pt/C at varying voltages, as determined by rotating ring-disk electrode (RRDE) measurements. The H_2O_2 yield and n of Co_3-NG are about 4.92% and 3.90, respectively, near to those of Pt/C (5.88% and 3.93), further verifying the predominant $4e^-$ process on the Co_3-NG. Furthermore, double layer capacitance (C_{dl}) and electrochemically active surface area (ECSA) of the samples were acquired by CV testing (Figures S14-S17 and Figure 3e).[42] The C_{dl} and ECSA values of Co_3-NG (16.3 mF cm^{-2} and 408 cm^2) are greater than those of Co_2-NG (12.5 mF cm^{-2} and 311 cm^2), Co_1-NG (7.6 mF cm^{-2} and 189 cm^2) and NG (2 mF cm^{-2} and 50 cm^2), indicating that Co_3-NG has larger electrochemical surface area, which exposes more ORR catalytic active sites. The fitted Nyquist plots reveal that the charge transfer resistance (R_{ct} = 4.1 Ω) of Co_3-NG is significantly lower than that of the other control catalysts (Figure S18). This indicates that Co_3-NG exhibits enhanced electron transfer capability and faster ORR kinetics. The high specific surface area and low charge transfer resistance of Co_3-NG further demonstrate its exceptional ORR performance.

For practical applications, stability and tolerance to methanol and CO are important indicators to measure the excellence of a catalyst.[35] Figure 3f shows that the current of the initial retention rate of Co_3-NG after 17 h is 93.8%, which surpasses that of Pt/C catalyst by a significant margin (only 73.1%), indicating excellent stability under alkaline conditions. Figure 3g depicts the current changes of Co_3-NG and Pt/C after adding methanol. The current change of Co_3-NG is negligible, while Pt/C drops sharply after adding methanol, and then slowly recovers to about 50%, implying that Co_3-NG has excellent cross-resistance to methanol. In addition, after continuing to inject 200 s CO into the solution, the current of the Co_3-NG catalyst is observed to decrease slightly, and then gradually

recover after stopping the CO injection, indicating that Co_3-NG exhibits superior CO tolerance to Pt/C (Figure S19).[43] The acidic ORR performance was evaluated in O_2-saturated 0.1 M $HClO_4$. Co_3-NG exhibits a half-wave potential of 0.74 V, slightly lower than Pt/C ($E_{1/2}$ = 0.77 V) (Figure S20a). However, Co_3-NG demonstrates superior durability, retaining 80.7% of its initial current after 6 h, far better than Pt/C, which remains only 61.6% under the same conditions (Figure S20b).

Then, the OER activity was evaluated in 1.0 M KOH. Co_3-NG demonstrates a voltage of 1.596 V at 10 mA cm^{-2} with η_{10} of 366 mV, which is minor than Co_2-NG (425 mV), Co_1-NG (479 mV) and commercial RuO_2 (397 mV) (Figure 3h). Besides, we also conducted chronoamperometric measurements, revealing that the current maintained near-constant levels after 14 hours of operation, further validating remarkable OER stability for the Co_3-NG (Figure 3i). The potential difference ΔE ($E_{j=10} - E_{1/2}$) on the oxygen electrode can be used to assess the bifunctional activity of the catalysts.[44] From Figure 3j, the ΔE of Co_3-NG is 0.693 V, surpassing that of Co_2-NG (0.8 V), Co_1-NG (0.875 V), Pt/C+RuO_2 (0.788 V) and most of the reported atomic catalysts (Figure S21), which indicates that Co_3-NG has better ORR/OER bifunctional catalytic performance.

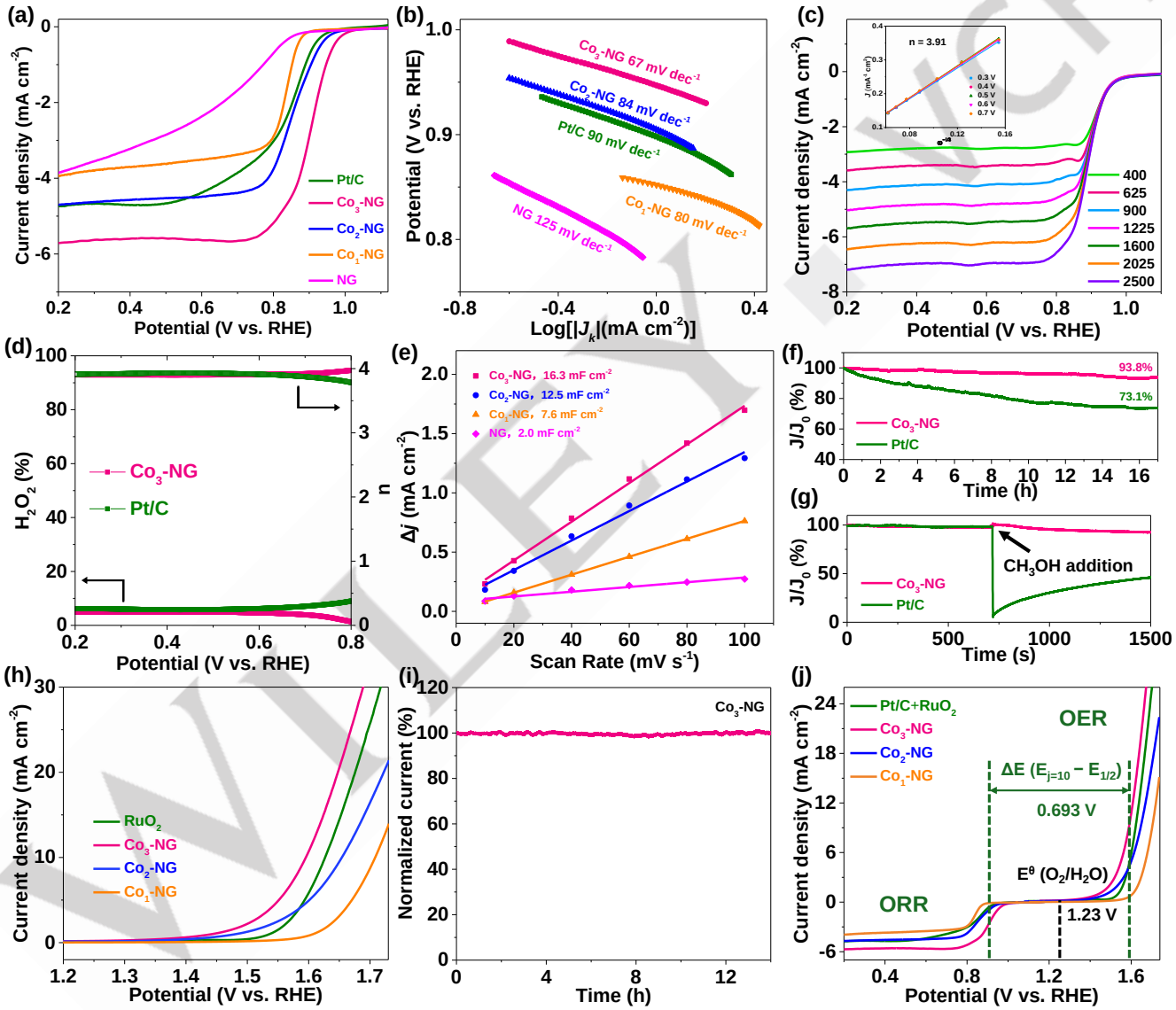

Figure 3. (a) ORR polarization curves. (b) Tafel slopes. (c) ORR polarization curves of Co_3-NG at various scanning rates (the inset: K–L plots). (d) H_2O_2 yields and n. (e) Capacitive current against the scan rate. (f) Stability evaluation at 0.5 V (vs. RHE). (g) Methanol tolerance tests (3 M). (h) OER LSV curves. (i) I-t curves of Co_3-NG. (j) OER/ORR bifunctional curves.

Studies on reaction mechanisms

To study the structural evolution of Co_3-NG during ORR, *in situ* XAS experiments were carried out.[45] We obtained the XAS spectra of Co_3-NG at different potentials in an O_2-saturated 0.1

M KOH solution. As depicted in Figure 4a, with the decrease of the applied potential, a change toward lower energy was detected in the absorption edge of Co_3-NG. Compared with open circuit potential (OCP) conditions, a pre-edge peak of reduced intensity was detected at 0.85 V and 0.80 V, indicating the occurrence of ORR.[46] Then, the EXAFS oscillations were used to detect structural changes at active sites throughout the ORR. The Co K-edge FT-EXAFS spectra indicate that the Co–N/O peak shifts from 1.51 to 1.69 Å during the reaction at 0.9 V, and the Co–O–Co signal shifts from 2.37 to 2.51 Å (Figure 4b), suggesting that the adsorption of intermediates at the active center causes the stretching of Co–N/O and Co–O–Co.[7] Furthermore, at different potentials, the intensity of Co–N/O and Co–O–Co varied to different degrees, potentially due to the reduction or oxidation of cobalt atoms and structural reconstruction. In addition, these changes are further influenced by the adsorption and desorption of reaction intermediates, exhibiting that the structure of Co_3ON_6 changes dynamically during the ORR.[47] The Co K-edge FT-EXAFS fitting results at different potentials demonstrate an enlarge in the coordination number of Co–N/O bonds, implying that Co atoms are the active centers for the ORR (Figure 4c-f and Table S2).[48] Additionally, Figure S22 displays the WT plots of Co_3-NG under various potentials, showing partial shifts in the Co–N/O and Co–O–Co scattering paths, further confirming that the Co atoms are the active sites for the ORR.[49] The *in situ* XAS analysis indicates that the catalytic ORR capability is directly associated with the active site of Co_3ON_6. In addition, we performed *in situ* Raman spectrum to detect the intermediates, and further identify potential active sites during ORR. In Figure S23, no obvious peaks were observed at an applied voltage of 1.1 V, signifying that the ORR did not occur. As the applied voltage decreases, two peaks appear at ~460 and ~615 cm^{-1}, assigned to $Co(OH)_2$ and CoOOH, respectively.[50] Meanwhile, the peak at ~910 cm^{-1} attributable with Co–O–Co, progressively becomes strong due to the adsorption of O intermediates with increasing potential.[51] Furthermore, the peaks emerged at ~1120 and ~1480 cm^{-1} can be ascribed to Co–*O_2 and Co–*OOH species, which forms via the adsorption of O_2 and *OOH species on the Co center.[52]

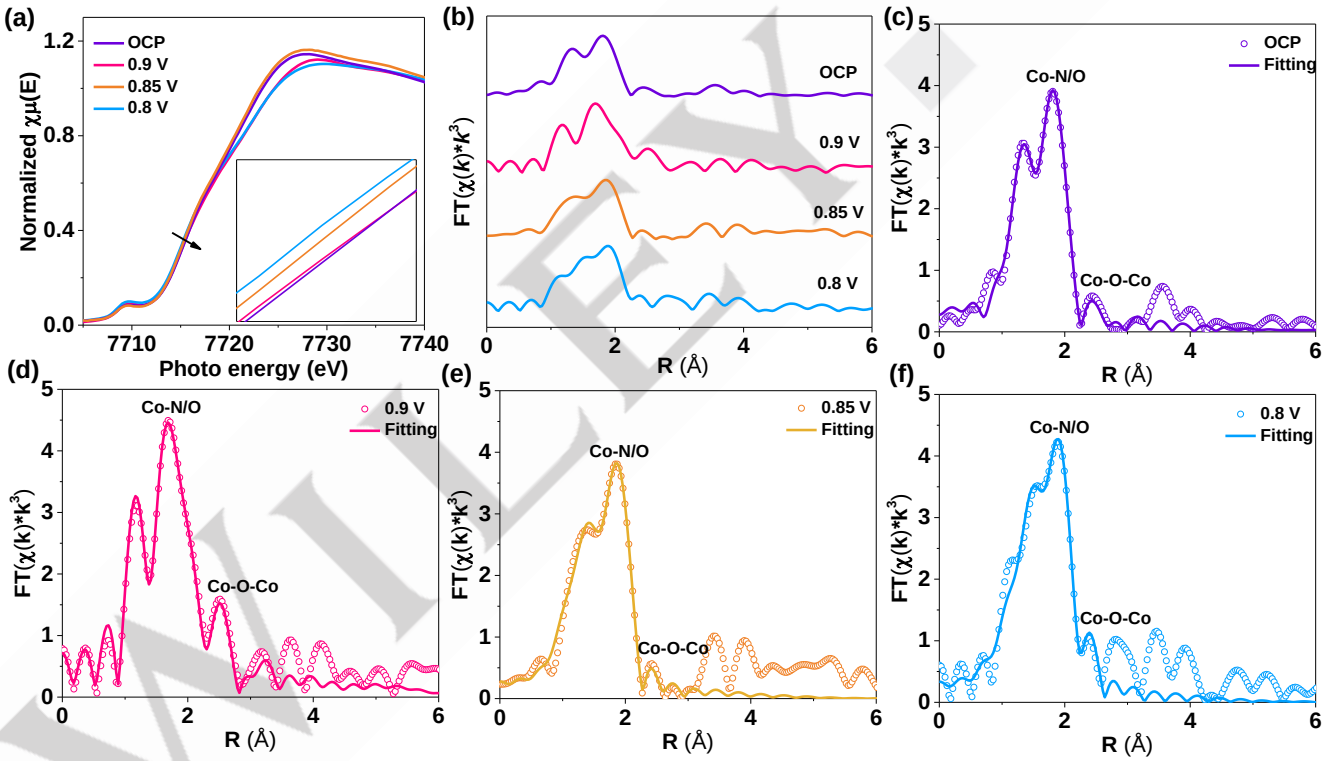

Figure 4. (a, b) In situ XANES and FT-EXAFS spectra of the Co k-edge at various potentials. (c-f) Co k-edge FT-EXAFS at OCP, 0.9, 0.85 and 0.8 V.

To acquire a deeper understanding of the ORR and OER mechanisms on the Co_3-NG materials, we conducted density functional theory (DFT) simulations. The optimized structure (Co_3ON_6) of Co_3-NG was built founded on the aforementioned AC-HAADF-STEM and XAFS findings (Figure S24a). For comparative purposes, models of Co_2-NG with a Co_2N_6 configuration and Co-NG with a CoN_4 configuration were also established (Figure S24b, c). Figure 5a, along with Figure S25a, b, illustrate the adsorption configurations of the optimized OOH*, O*, and OH* intermediates on Co_3-NG, Co_2-NG, and Co_1-NG. On Co_1-NG model, the intermediate adopts a cis-adsorption configuration on the Co–N_4 site. In the case of Co_2-NG, OOH* is cis-adsorbed on a single cobalt atom, while O* and OH* are bridge-adsorbed between two cobalt atoms. In contrast, the Co_3ON_6 active site in Co_3-NG offers a more diverse range of adsorption modes for these intermediates than Co_2-NG and Co_1-NG. Specifically, O* preferentially forms an axial connection through three Co–O bonds, one of which eventually breaks, leading to the formation of a bridging OH*.[53] The construction of the Co_3ON_6 active site provides a novel adsorption pathway for

ORR/OER intermediates. Figure 5b displays the change of Gibbs free energy (ΔG) during the ORR process. The rate-determining step (RDS) for all three configurations is the conversion of OH* to H_2O.[54] The ORR free energy diagram displays that each elementary step for three models is downhill at U = 0 V. The ΔG of Co_3-NG catalyst is 0.73 eV, surpassing that of Co_2-NG (0.60 eV) and Co_1-NG (0.48 eV), indicating that Co_3-NG is the most favorable to the ORR process.[55] When U = 1.23 V, the ΔG of each reaction step on the Co_3-NG is 0.08, −0.74, 0.16 and 0.50 eV, respectively. The desorption step of OH* is still the RDS with a lower energy barrier of 0.50 eV than on Co_2-NG (0.63 eV) and Co_1-NG (0.75 eV). These results underscore that Co_3-NG exhibits better ORR performance than Co_2-NG and Co_1-NG. Therefore, the synergistic effect of tri-atom cobalt and oxygen atoms optimizes the desorption energy of OH* and enhances the activity of ORR.

According to the Gibbs free energy diagram of OER process (Figure 5c), the RDS of Co_3-NG, Co_2-NG, and Co_1-NG are from *O to *OOH at U = 0 V, and the ΔG are 1.97, 2.12, and 2.22 eV, respectively. Notably, Co_3-NG has the smallest ΔG, indicating that it is most conducive to the OER. At U = 1.23 V, the overpotential of Co_3-NG is 0.74 eV, which is decreased compared to that on Co_2-NG (0.89 eV) and Co_1-NG (0.99 eV).[56] Furthermore, we explored and optimized other potential reaction pathways at the Co_3ON_6 active site, as illustrated in Figure S26. By calculating the ΔG values for ORR/OER associated with each pathway, we identified the pathway depicted in Figure 5(a) as the most thermodynamically favorable reaction mechanism. In summary, the Co_3-NG electrocatalyst can optimize the adsorption mode of the intermediates due to the unique arrangement of Co_3ON_6, which effectively regulates the adsorption/desorption energy of oxygen-containing intermediates, reduces the reaction energy barrier, and facilitates the progression of both ORR and OER.

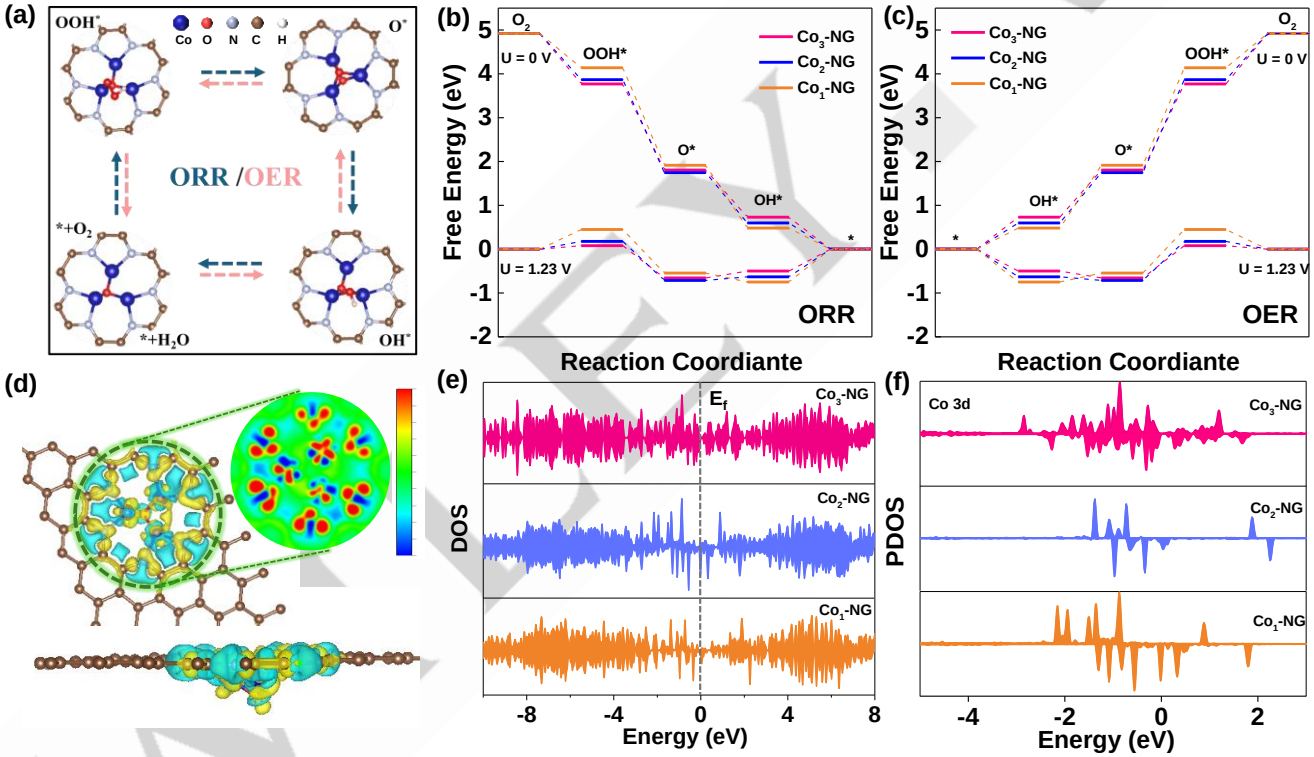

Figure 5. (a) The proposed ORR/OER mechanism on the Co_3-NG. (c, d) ΔG diagram of ORR and OER. (d) Charge density difference of Co_3-NG. (e, f) DOS and PDOS of Co 3d orbital in Co_3-NG, Co_2-NG and Co_1-NG.

The electron distribution in the Co_3-NG, Co_2-NG and Co_1-NG was studied by charge density difference. The electronegativity of O and N is bigger than that of Co, and electrons are easily obtained.[57] The construction of the triangular pyramidal Co_3ON_6 active site in the Co_3-NG triggers charge rearrangement and reduces the electron delocalization of Co_3-NG (Figure 5d and Figure S27). This rearrangement facilitates the swift release of electrons during reactions, thereby enhancing the dynamics of both ORR and OER.[58] To gain precise insights into the electronic effects of Co_3-NG, Co_2-NG, and Co_1-NG, we conducted calculations for the total density of states (DOS) and partial density of states (PDOS) for the three models, as depicted in Figure 5e, f. The d-band centers of Co_3-NG, Co_2-NG and Co_1-NG are −1.19 eV, −1.09 eV and −1.03 eV, respectively. A rightward shift in the d-band center moves the metal d-band closer to the Fermi level, enhancing the electronic interaction with adsorbates and typically increasing the adsorption energy. Conversely, a leftward shift has the opposite effect.[59] Notably, the d-band center of the Co_3-NG exhibited a notable leftward shift compared to those of Co_2-NG, and Co_1-NG

configurations. This shift reduced the electronic interaction between the Co_3ON_6 active site and the oxygen intermediates, thereby optimizing the adsorption energy.[60] Furthermore, the Co 3d-orbital of Co_3-NG occupies the largest electron state near the Fermi level, demonstrating that the triangular pyramidal Co_3ON_6 structure changes the electron density of the Co 3d-orbital, which is conducive to promoting the transfer between reaction intermediates and the active site.[61] The theoretical simulations show that Co_3-NG with triangular pyramidal Co_3ON_6 active site can effectively regulate the adsorption mode and d-band center of the reaction intermediates, decrease the reaction energy barriers, accelerate the reaction kinetics, and thus increase the ORR/OER activity.

Zn–air battery performance

By leveraging the exceptional ORR and OER performance of the Co_3-NG catalyst, it was incorporated into a rechargeable zinc-air battery (ZAB) to explore its potential practical application.[62] Specifically, the liquid rechargeable ZAB is assembled using Co_3-NG as the air cathode, a zinc plate as the anode, and 6 M KOH + 0.2 M $Zn(Ac)_2$ as the electrolyte (Figure 6a). The assembled ZAB with Co_3-NG obtains an open-circuit voltage (OCV) of 1.48 V, surpassing the OCV of a Pt/C+RuO_2-based ZAB (1.40 V), indicating its higher output voltage (Figure 6b). According to charge-discharge polarization curves (Figure 6c), the overall charge-discharge overpotential of Co_3-NG-based ZAB exhibits a minor voltage gap of 0.80 V at a large current density of 50 mA cm^{-2}, outperforming Pt/C+RuO_2 (1.22 V), suggesting the excellent performance of the Co_3-NG-based ZAB. Furthermore, discharge polarization curves and specific capacity curves (Figure 6d, e) demonstrates that the maximum power density and specific capacity of the Co_3-NG-based ZAB (189.0 mW cm^{-2} and 770.3 mAh g_{Zn}^{-1}) are superior to those of Pt/C+RuO_2 (146.5 mW cm^{-2} and 716.4 mAh g_{Zn}^{-1}). The Co_3-NG-based ZAB also performs better than recently reported Co-based atomic catalysts (Table S3). To evaluate the low-temperature performance of the Co_3-NG-assembled zinc-air battery, discharge curve tests were conducted at −20 °C, −10 °C, and 0 °C. As shown in the power density diagram (Figure S28), the corresponding maximum power density is 58.3, 72.6, and 118.7 mW cm^{-2}, respectively. These results highlight its low-temperature resistance under subzero conditions. Moreover, a comparison of discharge voltages at different current densities (5-50 mA cm^{-2}) shows that the discharge voltage and voltage recovery rate of the Co_3-NG-based ZAB are superior to the Pt/C+RuO_2-based ZAB, indicating that Co_3-NG-based ZAB has excellent discharge rates (Figure 6f). The stability of the Co_3-NG-based ZAB was evaluated as a vital indicator for practical applications (Figure 6g and Figure S29). The Co_3-NG-based ZAB exhibits a high energy efficiency of 56.41% and a low voltage gap of 0.85 V. Notably, after 3,000 cycles (500 h), the energy efficiency (54.64%) and voltage gap (0.88 V) displays minimal change, whereas the Pt/C+RuO_2-based ZAB demonstrates obvious degradation after 360 cycles (120 h), suggesting that Co_3-NG exhibits remarkable cycle stability. Additionally, a self-made flexible rechargeable ZAB using Co_3-NG as the cathode shows an OCV of 1.41 V, exceeding the OCV of a Pt/C+RuO_2-based flexible ZAB (1.33 V) (Figure 6h). In Figure 6i, the Co_3-NG-based flexible ZAB displays 10 h stability at 2 mA cm^{-2}, which is surpassed to the Pt/C+RuO_2-based flexible ZAB. Subsequently, the charge-discharge cycle constancy of the Co_3-NG-based flexible ZAB is experiment at folding angles of 0°, 90° and 180°, and the results indicate excellent flexibility and stability (Figure 6j).

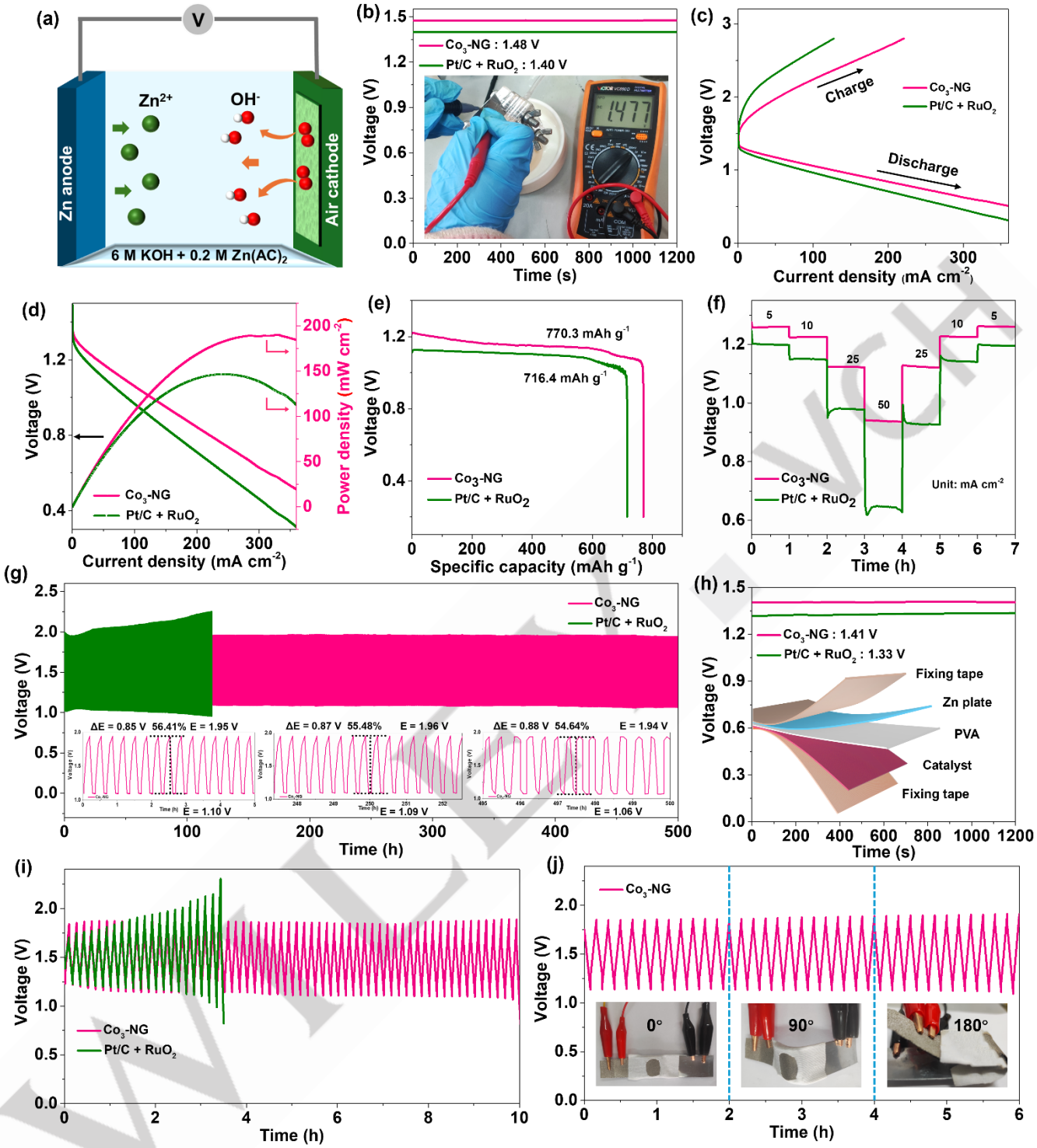

Figure 6. (a) Diagram of the ZAB. (b) OCV curves. (c) The Charge-discharge polarization curves. (d) The discharge polarization and power density curves. (e) Specific capacities at 10 mA cm^{-2}. (f) Constant discharge curve. (g) Cycling tests at 5 mA cm^{-2}. (h) OCV curves of the flexible ZAB. (i) Cycling tests at 2 mA cm^{-2}. (j) Cycling tests at 2 mA cm^{-2} by curving to 0°, 90°, and 180°.

Conclusion

In summary, Co_3-NG catalyst with triatomic cobalt sites has been successfully constructed by an ultrafast printing method, which is effective to increase the bifunctional ORR/OER activity. Triatomic cobalt sites were verified using AC-HAADF-STEM to directly observe and XAS experiments to analyze their coordination environment. The Co_3-NG is a durable and high-performance bifunctional catalyst in the electrocatalytic ORR ($E_{1/2}$ = 0.903 V) and OER (η_{10} = 366 mV), and the assembled zinc-air battery shows excellent operating performance and

excellent stability (3000 cycles), which results from intrinsic activity of Co_3ON_6 sites. Theoretical calculation results show that the Co_3ON_6 active site effectively modulates the ΔG of the rate-determining step, significantly accelerating the reaction kinetics and thereby enhancing the ORR/OER activity. In this work, the unique Co_3ON_6 active site in Co_3-NG offers multiple pathways for the adsorption of reaction intermediates, effectively breaking the linear scaling relationship typically observed between active sites and reaction intermediates in single-atom Co catalysts. Furthermore, the trigonal pyramidal structure of Co_3ON_6 modulates the electron density of the Co 3d orbital, enhancing the transfer of reaction intermediates between active sites. The synthesis method guarantees both high catalytic activity and exceptional stability of the catalyst. Therefore, the construction of the triatomic cobalt sites offers a novel perspective for the design of efficient bifunctional oxygen electrocatalyst and the study of the catalytic mechanism of oxygen electrocatalysis.

Supporting Information

The Supporting Information is available free.

Acknowledgements

This work was supported by the Natural Science Foundation of Jilin Province (No. 20220101051JC), and the National Natural Science Foundation of China (No. 22075099).

Keywords: Bifunctional electrocatalyst • Oxygen reduction reaction • Triatomic catalyst • *In situ* XAS • Rechargeable Zn-air battery

[1] W. Sun, F. Wang, B. Zhang, M. Zhang, V. Küpers, X. Ji, C. Theile, P. Bieker, K. Xu, C. Wang, M. Winter, *Science* **2021**, *371*, 46-51.

[2] X. Zhao, J. Chen, Z. Bi, S. Chen, L. Feng, X. Zhou, H. Zhang, Y. Zhou, T. Wågberg, G. Hu, *Adv. Sci.* **2023**, *10*, 2205889.

[3] a) T. Tang, Z. Wang, J. Guan, *Coord. Chem. Rev.* **2023**, *492*, 215288; b) C. Duan, J. Liu, Z. Li, R. Shi, J. Zhao, G. I. N. Waterhouse, X.-D. Wen, L.-P. Zhang, L.-Z. Wu, T. Zhang, *Adv. Mater.* **2025**, *37*, 2411648.

[4] a) L. Hu, C. Dai, L. Chen, Y. Zhu, Y. Hao, Q. Zhang, L. Gu, X. Feng, S. Yuan, L. Wang, B. Wang, *Angew. Chem. Int. Ed.* **2021**, *60*, 27324-27329; b) X. Zhang, H. Su, P. Cui, Y. Cao, Z. Teng, Q. Zhang, Y. Wang, Y. Feng, R. Feng, J. Hou, X. Zhou, P. Ma, H. Hu, K. Wang, C. Wang, L. Gan, Y. Zhao, Q. Liu, T. Zhang, K. Zheng, *Nat. Commun.* **2023**, *14*, 7115.

[5] Y. Zhao, H. Wu, Y. Wang, L. Liu, W. Qin, S. Liu, J. Liu, Y. Qin, D. Zhang, A. Chu, B. Jia, X. Qu, M. Qin, *Energy Storage Mater.* **2022**, *50*, 186-195.

[6] a) Q. Zhang, J. Guan, *Adv. Funct. Mater.* **2020**, *30*, 2000768; b) M. Chen, J. Guan, *Adv. Funct. Mater.* **2025**, 2423552.

[7] Y. Li, X. Luo, Z. Wei, F. Zhang, Z. Sun, Z. Deng, Z. Zhan, C. Zhao, Q. Sun, L. Zhang, W. Chen, S. Li, S. Pang, *Energy Environ. Sci.* **2024**, *17*, 4646-4657.

[8] M. Xiao, Y. Chen, J. Zhu, H. Zhang, X. Zhao, L. Gao, X. Wang, J. Zhao, J. Ge, Z. Jiang, S. Chen, C. Liu, W. Xing, *J. Am. Chem. Soc.* **2019**, *141*, 17763-17770.

[9] P. Guo, B. Liu, F. Tu, Y. Dai, Z. Zhang, Y. Xia, M. Ma, Y. Zhang, L. Zhao, Z. Wang, *Energy Environ. Sci.* **2024**, *17*, 3077-3087.

[10] J. Wang, Z. Huang, W. Liu, C. Chang, H. Tang, Z. Li, W. Chen, C. Jia, T. Yao, S. Wei, Y. Wu, Y. Li, *J. Am. Chem. Soc.* **2017**, *139*, 17281-17284.

[11] J. Zhong, Z. Liang, N. Liu, Y. Xiang, B. Yan, F. Zhu, X. Xie, X. Gui, L. Gan, H. B. Yang, D. Yu, Z. Zeng, G. Yang, *ACS Nano* **2024**, *18*, 5258-5269.

[12] T. Tang, X. Bai, Z. Wang, J. Guan, *Chem. Sci.* **2024**, *15*, 5082-5112.

[13] A. M. Roth-Zawadzki, A. J. Nielsen, R. E. Tankard, J. Kibsgaard, *ACS Catal.* **2024**, *14*, 1121-1145.

[14] W. Pei, S. Zhou, J. Zhao, X. Xu, Y. Du, S. X. Dou, *Nano Energy* **2020**, *76*, 105049.

[15] X. Shi, Y. Li, S. Zhang, R. Hu, S. Gao, P. Jin, J. Shang, J. Shui, *Nano Res.* **2023**, *16*, 8042-8050.

[16] X. Yan, D. Liu, P. Guo, Y. He, X. Wang, Z. Li, H. Pan, D. Sun, F. Fang, R. Wu, *Adv. Mater.* **2023**, *35*, 2210975.

[17] L. Wu, Y. Chen, C. Shao, L. Wang, B. Li, *Adv. Funct. Mater.* **2024**, 2408257.

[18] C. Walling, *Acc. Chem. Res.* **1975**, *8*, 125-131.

[19] a) T. Shen, X. Huang, S. Xi, W. Li, S. Sun, Y. Hou, *J. Energy Chem.* **2022**, *68*, 184-194; b) P. Kumar, K. Kannimuthu, A. S. Zeraati, S. Roy, X. Wang, X. Wang, S. Samanta, K. A. Miller, M. Molina, D. Trivedi, J. Abed, M. A. Campos Mata, H. Al-Mahayni, J. Baltrusaitis, G. Shimizu, Y. A. Wu, A. Seifitokaldani, E. H. Sargent, P. M. Ajayan, J. Hu, M. G. Kibria, *J. Am. Chem. Soc.* **2023**, *145*, 8052-8063; c) X. Wang, L. Xu, C. Li, C. Zhang, H. Yao, R. Xu, P. Cui, X. Zheng, M. Gu, J. Lee, H. Jiang, M. Huang, *Nat. Commun.* **2023**, *14*, 7210.

[20] Y.-X. Zhang, S. Zhang, H. Huang, X. Liu, B. Li, Y. Lee, X. Wang, Y. Bai, M. Sun, Y. Wu, S. Gong, X. Liu, Z. Zhuang, T. Tan, Z. Niu, *J. Am. Chem. Soc.* **2023**, *145*, 4819-4827.

[21] M. Moosavifar, A. Navid Arbat, M. Ranjbar, S. F. Hojati, *Iran. J. Sci. Technol. A* **2020**, *44*, 1387-1392.

[22] S. A. Chavan, D. Srinivas, P. Ratnasamy, *J. Catal.* **2001**, *204*, 409-419.

[23] T. Tang, Z. Duan, D. Baimanov, X. Bai, X. Liu, L. Wang, Z. Wang, J. Guan, *Nano Res.* **2023**, *16*, 2218-2223.

[24] H. Li, G. Yan, H. Zhao, P. C. Howlett, X. Wang, J. Fang, *Adv. Mater.* **2024**, *36*, 2311272.

[25] Y. Xue, Y. Guo, Q. Zhang, Z. Xie, J. Wei, Z. Zhou, *Nano-Micro Lett.* **2022**, *14*, 162.

[26] Y. Qi, Q. Liang, K. Song, X. Zhou, M. Liu, W. Li, F. Liu, Z. Jiang, X. Zou, Z. Chen, W. Zhang, W. Zheng, *J. Energy Chem.* **2024**, *95*, 306-314.

[27] H. Chang, X. Liu, S. Zhao, Z. Liu, R. Lv, Q. Zhang, T.-F. Yi, *Adv. Funct. Mater.* **2024**, *34*, 2313491.

[28] H. Huang, M. Sun, S. Li, S. Zhang, Y. Lee, Z. Li, J. Fang, C. Chen, Y.-X. Zhang, Y. Wu, Y. Che, S. Qian, W. Zhu, C. Tang, Z. Zhuang, L. Zhang, Z. Niu, *J. Am. Chem. Soc.* **2024**, *146*, 9434-9443.

[29] a) H. Chang, L. Zhao, S. Zhao, Z.-L. Liu, P.-F. Wang, Y. Xie, T.-F. Yi, *J. Energy Chem.* **2024**, *93*, 400-410; b) H. Chang, Y.-F. Guo, X. Liu, P.-F. Wang, Y. Xie, T.-F. Yi, *Appl. Catal., B* **2023**, *327*, 122469.

[30] Y.-X. Zhao, J.-H. Wen, P. Li, P.-F. Zhang, S.-N. Wang, D.-C. Li, J.-

M. Dou, Y.-W. Li, H.-Y. Ma, L. Xu, *Angew. Chem. Int. Ed.* **2023**, *62*, e202216950.

[31] T. Tang, W.-J. Jiang, X.-Z. Liu, J. Deng, S. Niu, B. Wang, S.-F. Jin, Q. Zhang, L. Gu, J.-S. Hu, L.-J. Wan, *J. Am. Chem. Soc.* **2020**, *142*, 7116-7127.

[32] K. R. Yoon, C.-K. Hwang, S.-h. Kim, J.-W. Jung, J. E. Chae, J. Kim, K. A. Lee, A. Lim, S.-H. Cho, J. P. Singh, J. M. Kim, K. Shin, B. M. Moon, H. S. Park, H.-J. Kim, K. H. Chae, H. C. Ham, I.-D. Kim, J. Y. Kim, *ACS Nano* **2021**, *15*, 11218-11230.

[33] S. Huang, D. Tranca, F. Rodríguez-Hernández, J. Zhang, C. Lu, J. Zhu, H.-W. Liang, X. Zhuang, *Angew. Chem. Int. Ed.* **2024**, *63*, e202314833.

[34] T. Sun, W. Zang, H. Yan, J. Li, Z. Zhang, Y. Bu, W. Chen, J. Wang, J. Lu, C. Su, *ACS Catal.* **2021**, *11*, 4498-4509.

[35] M. Liu, X. Wang, S. Cao, X. Lu, W. Li, N. Li, X.-H. Bu, *Adv. Mater.* **2024**, *36*, 2309231.

[36] Z. Pei, H. Zhang, Y. Guo, D. Luan, X. Gu, X. W. Lou, *Adv. Mater.* **2023**, 2306047.

[37] G. Yang, M. Fan, Q. Liang, X. He, W. Zhang, T. Asefa, *Angew. Chem. Int. Ed.* **2024**, e202421168.

[38] W. Si, Z. Yang, X. Hu, Q. Lv, X. Li, F. Zhao, J. He, C. Huang, *J. Mater. Chem. A* **2021**, *9*, 14507-14514.

[39] X. Wei, S. Song, W. Cai, X. Luo, L. Jiao, Q. Fang, X. Wang, N. Wu, Z. Luo, H. Wang, Z. Zhu, J. Li, L. Zheng, W. Gu, W. Song, S. Guo, C. Zhu, *Chem* **2023**, *9*, 181-197.

[40] H. T. Chung, D. A. Cullen, D. Higgins, B. T. Sneed, E. F. Holby, K. L. More, P. Zelenay, *Science* **2017**, *357*, 479-484.

[41] Y. Wang, J. Wu, S. Tang, J. Yang, C. Ye, J. Chen, Y. Lei, D. Wang, *Angew. Chem. Int. Ed.* **2023**, *62*, e202219191.

[42] H. Zhang, H.-C. Chen, S. Feizpoor, L. Li, X. Zhang, X. Xu, Z. Zhuang, Z. Li, W. Hu, R. Snyders, D. Wang, C. Wang, *Adv. Mater.* **2024**, *36*, 2400523.

[43] T. Tang, Y. Wang, J. Han, Q. Zhang, X. Bai, X. Niu, Z. Wang, J. Guan, *Chin. J. Catal.* **2023**, *46*, 48-55.

[44] S. Cai, Z. Meng, H. Tang, Y. Wang, P. Tsiakaras, *Appl. Catal., B* **2017**, *217*, 477-484.

[45] Y. Yang, Y. Wang, Y. Xiong, X. Huang, L. Shen, R. Huang, H. Wang, J. P. Pastore, S.-H. Yu, L. Xiao, J. D. Brock, L. Zhuang, H. D. Abruña, *J. Am. Chem. Soc.* **2019**, *141*, 1463-1466.

[46] J. Gu, C.-S. Hsu, L. Bai, M. Chen Hao, X. Hu, *Science* **2019**, *364*, 1091-1094.

[47] N. Zhang, T. Zhou, J. Ge, Y. Lin, Z. Du, C. a. Zhong, W. Wang, Q. Jiao, R. Yuan, Y. Tian, W. Chu, C. Wu, Y. Xie, *Matter* **2020**, *3*, 509-521.

[48] Z. Sun, C. Li, Z. Wei, F. Zhang, Z. Deng, K. Zhou, Y. Wang, J. Guo, J. Yang, Z. Xiang, P. Ma, H. Zhai, S. Li, W. Chen, *Adv. Mater.* **2024**, *36*, 2404665.

[49] Z. Sun, X. Luo, H. Shang, Z. Wang, L. Zhang, W. Chen, *Angew. Chem. Int. Ed.* **2024**, e202405778.

[50] B. Sun, S. Zhang, H. Yang, T. Zhang, Q. Dong, W. Zhang, J. Ding, X. Liu, L. Wang, X. Han, W. Hu, *Adv. Funct. Mater.* **2024**, *34*, 2315862.

[51] X. Lin, D. Liu, L. Shi, F. Liu, F. Ye, R. Cheng, L. Dai, *Small* **2024**, 2407146.

[52] Y. Wang, P. Meng, Z. Yang, M. Jiang, J. Yang, H. Li, J. Zhang, B. Sun, C. Fu, *Angew. Chem. Int. Ed.* **2023**, *62*, e202304229.

[53] T. Lu, Q. Zhou, J. Li, T. Li, J. Gong, S. Zhang, H. Pang, S. Xi, L. Xu, G. Luo, D. Sun, K. Sun, Y. Tang, *Adv. Funct. Mater.* **2024**, *34*, 2405564.

[54] Y. Chen, J. Mao, H. Zhou, L. Xing, S. Qiao, J. Yuan, B. Mei, Z. Wei, S. Zhao, Y. Tang, C. Liu, *Adv. Funct. Mater.* **2024**, *34*, 2311664.

[55] S. Zhao, M. Liu, Z. Qu, Y. Yan, Z. Zhang, J. Yang, S. He, Z. Xu, Y. Zhu, L. Luo, K. N. Hui, M. Liu, J. Zeng, *Angew. Chem. Int. Ed.* **2024**, e202408914.

[56] J. Qiao, Y. You, L. Kong, W. Feng, H. Zhang, H. Huang, C. Li, W. He, Z. Sun, *Adv. Mater.* **2024**, *36*, 2405533.

[57] Y. Li, Y. Ding, B. Zhang, Y. Huang, H. Qi, P. Das, L. Zhang, X. Wang, Z.-S. Wu, X. Bao, *Energy Environ. Sci.* **2023**, *16*, 2629-2636.

[58] H. Hu, J. Wang, B. Cui, X. Zheng, J. Lin, Y. Deng, X. Han, *Angew. Chem. Int. Ed.* **2022**, *61*, e202114441.

[59] J. Greeley, J. K. Nørskov, *Surf. Sci.* **2007**, *601*, 1590-1598.

[60] a) E. Zhu, T. Zheng, J. Yu, C. Shi, L. Zhou, H. Jin, J. Yang, G. Luo, D. Wei, X. Yang, M. Xu, *Energy Storage Mater.* **2024**, *69*, 103410; b) Z. Wang, L. Shang, H. Yang, Y. Zhao, G. I. N. Waterhouse, D. Li, R. Shi, T. Zhang, *Adv. Mater.* **2023**, *35*, 2303818.

[61] S. Chandrasekaran, R. Hu, L. Yao, L. Sui, Y. Liu, A. Abdelkader, Y. Li, X. Ren, L. Deng, *Nano-Micro Lett.* **2023**, *15*, 48.

[62] H. Yang, S. Gao, D. Rao, X. Yan, *Energy Storage Mater.* **2022**, *46*, 553-562.

10.1002/anie.202503019

Entry for the Table of Contents

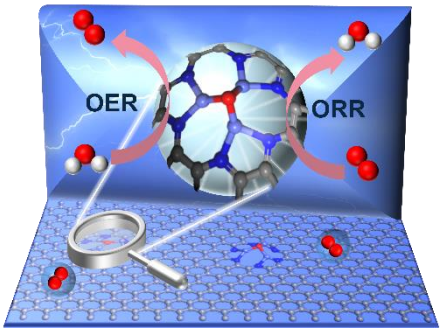

Using an ultrafast printing technique, we have successfully embedded triatomic cobalt cluster precursors into graphene nanosheets, resulting in a triatomic Co_3-NG catalyst with excellent bifunctional OER/ORR activity. The triangular pyramidal active sites effectively regulate the d-band center and electronic structure, and promote the adsorption/desorption of oxygen intermediates.